Diffuse-interface approach to rotating Hele-Shaw flows

Ching-Yao Chen[*] and Yu-Sheng Huang

Department of Mechanical Engineering, National Chiao Tung University, Hsinchu, Taiwan 30010, Republic of China

José A. Miranda[†]

Departamento de Física, Universidade Federal de Pernambuco, Recife PE 50670-901, Brazil

When two fluids of different densities move in a rotating Hele-Shaw cell, the interface between them becomes centrifugally unstable and deforms. Depending on the viscosity contrast of the system, distinct types of complex patterns arise at the fluid-fluid boundary. Deformations can also induce the emergence of interfacial singularities and topological changes such as droplet pinch-off and self-intersection. We present numerical simulations based on a diffuse-interface model for this particular two-phase displacement that capture a variety of pattern-forming behaviors. This is implemented by employing a Boussinesq Hele-Shaw-Cahn-Hilliard approach, considering the whole range of possible values for the viscosity contrast, and by including inertial effects due to the Coriolis force. The role played by these two physical contributions on the development of interface singularities is illustrated and discussed.

I. INTRODUCTION

Rotating Hele-Shaw flows have been the subject of considerable interest during the last two decades. This particular type of confined flow offers a variation to the traditional viscosity-driven Saffman-Taylor problem [1,2]. It occurs when a fluid, surrounded by another of lower density, is located in a Hele-Shaw cell, which rotates about a perpendicular axis. Inertial forces act upon the density difference between the fluids, and a density-driven instability results [3].

Since the seminal works by Schwartz [4], and Carrillo *et al.* [5], various aspects of the rotating Hele-Shaw problem have been investigated both theoretically and experimentally, mostly focusing on comprehending the complex morphology and dynamics of emerging interfacial patterns. These studies include the development of time-dependent [6–9] and stationary [10,11] exact solutions, the consideration of miscible fluid displacements [12,13], the dependence of pattern morphologies on viscous [14–16] and wetting [17] effects, and the influence of the Coriolis force on the interfacial dynamics [18–21].

The rotating flow fingering patterns obtained by experiments exhibit a rich collection of shapes: they may change from teardrop-like structures to thin filamented arms presenting swelled ends, or to a branched, backbone architecture with nearly constant finger widths. Complicated pinch-off phenomena are also detected, characterizing the formation of satellite droplets, which are detached from the main body of the denser fluid [14,22].

On the theoretical side, state-of-the-art numerical simulations are utilized to successively reproduce experimental pattern-forming morphologies: (i) on one hand, boundary integral techniques [16,20] and conformal mapping approaches [23] model immiscible displacements, while (ii) spectral methods [12,13] are used when the fluids are miscible. These numerical studies have verified that the viscosity contrast

$-1 \leqslant A \leqslant 1$ (dimensionless viscosity difference between the fluids) plays a crucial role in determining the resulting patterned structures, in the sense that finger competition dynamics changes significantly when the magnitude and sign of A is varied.

A recent numerical study [22] used phase-field simulations based on a vortex-sheet formalism [24–26] to model the occurrence of the experimentally observed interfacial pinch-off events, and examined how they are modified as A varies from 0 to 1, in the absence of Coriolis effects. Consistently with their own experimental observations, it has been found that pinch-off singularities are more frequent when $A \to 0$.

Phase-field (or, diffuse-interface) modeling [24–36] offers a convenient alternative to usual sharp-interface approaches (e.g., boundary-integral and conformal mapping methods), which can not handle interface topological changes such as finger pinch-off and merging. In the framework of the diffuse-interface theory, the fluid-fluid boundary is represented by a thin layer of finite thickness, and not as a sharp interface. The main idea underlying this theory is to introduce an auxiliary function (the phase-field function) that indicates in which "phase" (here, in which fluid) the system is at a given point. It assumes different values in the bulk phase away from the interfacial region, through which the phase function varies rapidly, but smoothly from one phase to another. Hence, the difficulty of dealing with discontinuities at the interface is naturally avoided. In this context, the interface itself can be associated with an intermediate contour set of the phase function. There has been much work on the employment of diffuse-interface models in multicomponent fluid flows. We refer the reader to the classic review [27] and references therein for a vast literature on this topic.

In this paper, we consider a diffuse-interface approach that is based on a simplified version of the Navier-Stokes-Cahn-Hilliard model [28–31], originally applied to two-phase fluid flow in motionless (nonrotating) Hele-Shaw cells [32–35]. We extend the results obtained in Refs. [32–35] to the rotating Hele-Shaw setup, and used intensive numerical simulations to analyze the fully nonlinear behavior of the evolving interfacial

---

[*]chingyao@mail.nctu.edu.tw
[†]jme@df.ufpe.br

patterns. Notice that our theoretical approach differs from the one adopted in Ref. [22] in the sense that diffusion effects between the fluid components provide a relevant physical mechanism to smooth flow discontinuities (for details, see Ref. [32]). It is also worth mentioning that our analysis is done by spanning all possible signs for the viscosity contrast ($A > 0$, $A = 0$, and $A < 0$), and by taking Coriolis force effects into account.

In other words, in contrast to our previous numerical investigations of the (miscible and immiscible) rotating Hele-Shaw problem [12,13,16,20,21,23], here we employ a Boussinesq Hele-Shaw-Cahn-Hilliard description that is able to accurately model the occurrence of topological singularities at a diffuse interface (pinch-off and coalescence of fingers). Among other things, this allowed us to understand how the emergence of such singularities is influenced by the effects of viscosity contrast (including $A < 0$) and Coriolis force.

This paper consists of three additional sections. Section II is devoted to introduce the setup of the physical problem, the application of the diffuse-interface formalism to rotating Hele-Shaw flows, and the related governing equations. Section III presents our numerical results. Numerical experiments in the absence of Coriolis effects are exhibited in Sec. III A, revealing a number of relevant interfacial structures as the viscosity contrast is varied from negative to positive values. These results also serve to validate our numerical approach and to support the effectiveness of the proposed diffuse-interface method. The way pattern formation and the occurrence of finger pinch-off and self-intersection respond to Coriolis effects is discussed in Sec. III B. Finally, Sec. IV summarizes our main conclusions.

II. PHYSICAL PROBLEM AND GOVERNING EQUATIONS

We investigate the interfacial instability between two immiscible fluids in a rotating Hele-Shaw cell (Fig. 1). The cell has gap spacing h and turns around an axis perpendicular to the plane of the flow with constant angular velocity Ω. Inside the cell, an initially circular drop (radius R_0) of fluid 2 is surrounded by an outer fluid 1. The densities and viscosities of the fluids are denoted by ρ_j and η_j, respectively ($j = 1,2$). We focus on the centrifugally induced motion where $\rho_2 > \rho_1$, but allow the inner fluid to be either more or less viscous than
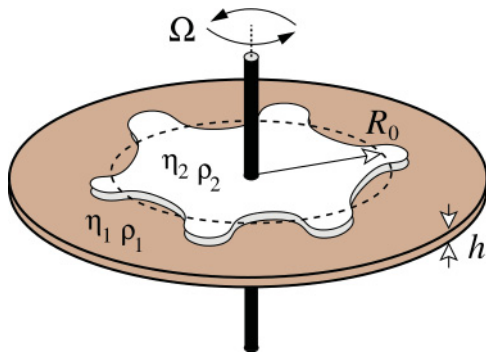

FIG. 1. (Color online) Sketch of a rotating Hele-Shaw cell of gap width h. It spins around a perpendicular axis passing through its center, with angular velocity Ω. The inner fluid is denser ($\rho_2 > \rho_1$) so that the initially circular fluid-fluid interface of radius R_0 distorts.

the outer fluid. We examine situations in which the viscosity contrast can assume negative, null, and positives values.

The governing equations of such a diffuse interface problem are based on a model proposed by Cahn and Hilliard [28]. In the context of a rotating Hele-Shaw cell system, the equations can be written as [4,32,36]

$$\frac{\partial \rho}{\partial t} + \nabla \cdot (\rho \mathbf{u}) = 0, \tag{1}$$

$$\nabla p = -\frac{12\eta}{h^2}\mathbf{u} + \rho\Omega^2\mathbf{r} + 2\rho\Omega(\mathbf{e_z} \times \mathbf{u})$$
$$- \epsilon\nabla \cdot [\rho(\nabla c)(\nabla c)^T], \tag{2}$$

$$\rho\left(\frac{\partial c}{\partial t} + \mathbf{u}\cdot\nabla c\right) = \alpha\nabla^2\mu, \tag{3}$$

$$\mu = \frac{\partial f_0}{\partial c} - \frac{\epsilon}{\rho}\nabla \cdot (\rho\nabla c) - \frac{p}{\rho^2}\frac{d\rho}{dc}, \tag{4}$$

$$f_0 = f^*c^2(1 - c)^2. \tag{5}$$

Here, $\mathbf{u}$ denotes the fluid velocity vector, p the pressure, η the viscosity, and ρ the density of the binary fluid system. The phase-field variable is represented by c, so that $c = 1$ in the bulk of fluid 1 (phase 1) and $c = 0$ in the bulk of fluid 2 (phase 2). The constants ϵ and α represent the coefficient of capillarity and mobility, respectively. The chemical potential is denoted by μ, and f_0 is a free energy (or, the Helmholtz free energy) with a characteristic specific energy f^*. Notice the inclusion of both centrifugal and Coriolis force terms in the generalized Darcy's law (2), where $\mathbf{r}$ is the radial position vector, and $\mathbf{e_z}$ represents the unit vector along the rotation axis (z axis). Equations (1)–(5) define the so-called Hele-Shaw-Cahn-Hilliard model [32,34] associated with a surface free energy functional given by

$$E = \rho\int\left(f_0 + \frac{\epsilon}{2}(\nabla c)^2\right)dV, \tag{6}$$

where V is the volume of the fluid domain.

It is worth noticing that the choice of free energy leads to different interpretations of the model [32]. The present choice of a quartic free energy f_0 indicates the phases are separated, so that is suitable for an immiscible interface. If a convex free energy $f_0 = 0.5(c - 0.5)^2$ is applied, fluid diffusion is allowed. By further assuming an extremely small ϵ, so that $\mu = \partial f_0/\partial c$, the method becomes similar to the one used in miscible simulations, including Korteweg stresses [13,21,37,38].

Correlations of viscosity (η) and density (ρ) with the phase-field variable c are required by the present approach. To take advantage of the highly accurate scheme previously developed for miscible Hele-Shaw flows [39–41], we assume that

$$\eta(c) = \eta_1 e^{[R(1-c)]}, \quad R = \ln\left(\frac{\eta_2}{\eta_1}\right), \tag{7}$$

$$\rho(c) = \rho_1 c + \rho_2(1 - c). \tag{8}$$

For immiscible flow situations, the form of the correlation between the phase-field variable c and viscosity η such as the one shown in (7) is aimed to provide a smooth variation of viscosity between the two fluids within the diffuse interface. In the early studies of phase-field simulations, a simpler

linear proportionality rule was commonly used. However, our numerical code is originated from the schemes designed to a miscible interface, where a more physical correlation would be desired. The specific functional form given by Eq. (7) has been originally proposed some time ago in a seminal paper by Tan and Homsy [42]. The validity and suitability of this expression has been extensively demonstrated by contrasting numerical simulations [39–41] and experiments [43–45] for various combinations of fluids. To take advantage of the high accuracy associated with such miscible schemes, a similar exponential correlation is utilized in this work.

If a Boussinesq approximation is applied, the density can be represented by a constant bulk density ρ_b, except in the centrifugal term. In order to render the governing equations dimensionless, the initial radius of the inner fluid drop R_0 and density difference $\Delta\rho = \rho_2 - \rho_1$ are taken as characteristic scales. Viscosities and time are scaled by η_1 and $12\eta_1/(\Delta\rho\Omega^2 h^2)$, respectively. In conjunction with a characteristic velocity $(\Delta\rho\Omega^2 R_0 h^2)/12\eta_1$, pressure $\Delta\rho\Omega^2 R_0^2$, and specific free energy f_0^*, the dimensionless Boussinesq Hele-Shaw-Cahn-Hilliard (BHSCH) equations [32,34] associated to Eqs. (1)–(5) can be written as

$$\nabla \cdot \mathbf{u} = 0, \tag{9}$$

$$\nabla p = -\eta\mathbf{u} - \left(c + \frac{\rho_2}{\Delta\rho}\right)[\mathbf{r} + 2\,\mathrm{Re}(\mathbf{e_z} \times \mathbf{u})]$$
$$- \frac{C}{\mathrm{Ga}}\nabla \cdot [(\nabla c)(\nabla c)^T], \tag{10}$$

$$\frac{\partial c}{\partial t} + \mathbf{u}\cdot\nabla c = \frac{1}{\mathrm{Pe}}\nabla^2\mu, \tag{11}$$

$$\mu = \frac{\partial f_0}{\partial c} - C\nabla^2 c, \tag{12}$$

$$f_0 = c^2(1 - c)^2. \tag{13}$$

Dimensionless parameters, such as the Péclet number Pe, the viscosity contrast A, the Cahn number C, the rotationally modified Galileo number Ga, and the (Coriolis force related) Reynolds number Re are defined as

$$\mathrm{Pe} = \frac{\rho_b\Delta\rho\Omega^2 h^2 R_0^2}{12\alpha\eta_1 f^*}, \quad A = \frac{e^R - 1}{e^R + 1}, \quad C = \frac{\epsilon}{f^* R_0^2},$$

$$\mathrm{Ga} = \frac{\Delta\rho\Omega^2 R_0^2}{\rho_b f^*}, \quad \mathrm{Re} = \frac{\Delta\rho\Omega h^2}{12\eta_1}.$$

Moreover, the dimensionless free interfacial energy corresponding to Eq. (6) can be obtained accordingly as

$$E = \frac{1}{\mathrm{Ga}}\int\left(f_0 + \frac{C}{2}(\nabla c)^2\right)dV. \tag{14}$$

In order to solve the governing equations numerically, we recast them into the well known stream function vorticity formulation (ϕ, ω) [39], yielding

$$u = \frac{\partial\phi}{\partial y}, \quad v = -\frac{\partial\phi}{\partial x} \tag{15}$$

$$\nabla^2\phi = -\omega, \tag{16}$$

where

$$\omega = -R\left(u\frac{\partial c}{\partial y} - v\frac{\partial c}{\partial x}\right) - \frac{1}{\eta}\left(y\frac{\partial c}{\partial x} - x\frac{\partial c}{\partial y}\right)$$
$$- \frac{2\,\mathrm{Re}}{\eta}\left(u\frac{\partial c}{\partial x} + v\frac{\partial c}{\partial y}\right)$$
$$+ \frac{C}{\eta\mathrm{Ga}}\left[\frac{\partial c}{\partial x}\left(\frac{\partial^3 c}{\partial x^2\partial y} + \frac{\partial^3 c}{\partial y^3}\right) - \frac{\partial c}{\partial y}\left(\frac{\partial^3 c}{\partial x\partial y^2} + \frac{\partial^3 c}{\partial x^3}\right)\right].$$

As in Refs. [14,16,22], a dimensionless rotational Bond number, defined as $\mathrm{Bo} = \sigma/\Delta\rho\Omega^2 R_0^3$, can be used to evaluate the ratio between the capillary and centrifugal forces. If a one-dimensional interface (associated with a given spatial variable ζ) is assumed, the surface tension (or, free energy) can be calculated as

$$\sigma = \frac{1}{\mathrm{Ga}}\int\left[f_0 + \frac{C}{2}\left(\frac{\partial c}{\partial\zeta}\right)^2\right]d\zeta. \tag{17}$$

Under such circumstances, an equilibrium surface tension equation can be obtained as [30]

$$\frac{C}{2}\left(\frac{\partial c}{\partial\zeta}\right)^2 = c^2(1 - c)^2. \tag{18}$$

If we further assume a boundary condition of an average value of the phase-field variable at the midpoint of the interface, i.e., $c(0) = 1/2$, the distribution of phase-field variable can be solved analytically as

$$c = \frac{e^{(\sqrt{\frac{2}{C}})\zeta}}{1 + e^{(\sqrt{\frac{2}{C}})\zeta}}. \tag{19}$$

Considering all this, an equilibrium rotational Bond number can be defined as

$$\mathrm{Bo}_e = \frac{\sqrt{C/2}}{3\mathrm{Ga}}. \tag{20}$$

Boundary conditions are prescribed as follows:

$$x = \pm 1 : \phi = 0, \quad \frac{\partial c}{\partial x} = 0, \quad \frac{\partial^2 c}{\partial x^2} = 0, \tag{21}$$

$$y = \pm 1 : \phi = 0, \quad \frac{\partial c}{\partial y} = 0, \quad \frac{\partial^2 c}{\partial y^2} = 0. \tag{22}$$

To reproduce the extremely fine structures of the fingers, a highly accurate pseudospectral method is employed. As a result, the actual boundary conditions applied in the numerical code are $\partial\phi/\partial y = 0$ at $y = \pm 1$. However, at the present situation where no concentration gradient is generated on the boundaries, the above conditions automatically lead to $\phi = 0$. To ensure this condition, all the simulations are terminated when the inner fluid reaches a certain distance away from the computational boundaries. Both c and ϕ are expanded in a cosine series in the x direction. In the y direction, discretization is accomplished by sixth order compact finite differences. Time integration is fully explicit and utilizes a third order Runge-Kutta procedure. The evaluation of the nonlinearity at each time level is performed in a pseudospectral manner. For a more detailed account about these numerical schemes, the reader is referred to Refs. [39–41].

At this point, we believe some clarifications about the discretization schemes along the x-y directions are necessary.

At first glance, by considering the circular geometry and overall symmetry of the physical problem under study, it may seem obvious that the most appropriate theoretical description would obligatorily involve the use of a polar coordinate system (r, θ). However, this is not exactly the case when an accurate numerical description of the problem needs to be implemented.

In order to successfully generate the extremely fine and intricate fingering structures emerging in the rotating Hele-Shaw problem, a highly accurate numerical scheme is required. To accomplish this task, spectral methods associated with discretization by high order compact finite difference schemes are a very useful tool. In practice, the use of such spectral methods, which require periodic boundaries in one direction, and of compact finite difference schemes, which perform better in a uniform grid, impose serious limitations on the implementation of a numerical code based on polar coordinates. In this sense, the ability of generating extremely fine patterning structures is somewhat incompatible (or at least, much more difficult) with the eventual choice of polar coordinates.

This is why we have adopted a rectangular coordinate system (x, y) to describe our current problem. A similar procedure has been very successfully applied in Ref. [13], which describes the miscible displacement in rotating Hele-Shaw flows. The excellent agreements (both qualitative and quantitative) with existing experiments and other numerical approaches obtained in this work and in Ref. [13] support the applicability, reliability, and general appropriateness for our choice of Cartesian coordinates.

III. NUMERICAL RESULTS AND DISCUSSION

A. Fingering dynamics in the absence of the Coriolis force

In this section, we introduce numerical results for rotating Hele-Shaw flows that neglect Coriolis force effects. We begin by presenting data related to various numerical experiments (more than 40) considering a wide range of values for the relevant control parameters: $Pe = 10^3$, 3×10^3, 6×10^3, 9×10^3, 1.2×10^4; $A = -0.76$, 0, 0.25, 0.46, 0.76; $Ga = 0.1, 0.4, 1, 2, 10$; and $C = 10 \times 10^{-5}$.

From Eq. (20), these values of Ga and C result in five major groups for the equilibrium rotational Bond number Bo_e: (a) 7.45×10^{-5}, (b) 3.73×10^{-4}, (c) 7.45×10^{-4}, (d) 7.45×10^{-3}, and (e) 1.86×10^{-3}. A representative sample of fingering patterns associated to groups (a)–(d) is depicted in the insets of Fig. 2, which plot the number of fingers N as a function of Bo_e. The solid curve represents the relation $N \approx \sqrt{(1/3Bo)}$ obtained analytically in Ref. [5] through linear stability analysis.

The images shown in the insets (a)–(d) of Fig. 2 clearly illustrate prominent fingering patterns with well defined interfaces, presenting minimal dispersion. It is evident that smaller values of Bo_e (meaning small surface tension, or large centrifugal driving) lead to patterns presenting a larger number of fingering structures. Another clear feature is the favored occurrence of droplet emissions at the finger tips when Bo_e is decreased. These simulated morphological attributes agree very well with existing experiments [5,14,17,22], as well as with other numerical simulations based on boundary integral methods [14,16] and phase-field modeling based on
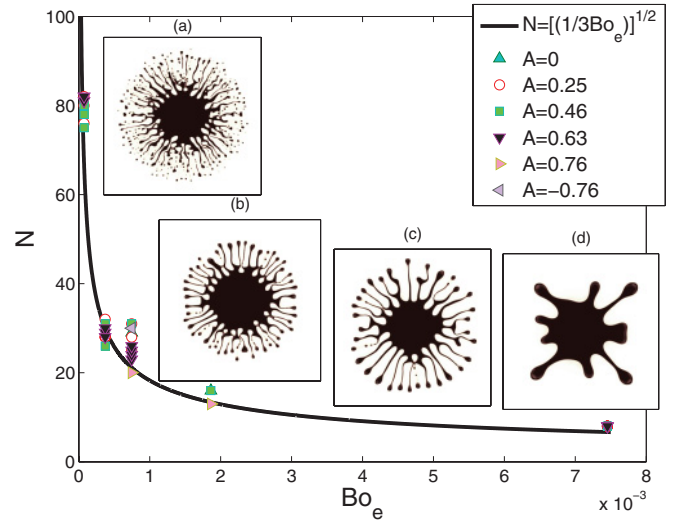

FIG. 2. (Color online) Number of fingers N plotted as a function of the equilibrium rotational Bond number Bo_e. The solid curve represents the analytical relationship $N \approx \sqrt{1/3Bo_e}$, and the symbols indicate data obtained from our numerical experiments. The specific parameters used to obtain the fully nonlinear fingering patterns shown in the insets are (a) $Pe = 3 \times 10^3$, $A = 0.63$, $Ga = 10$, and $C = 10^{-5}$ ($Bo_e = 7.45 \times 10^{-5}$); (b) $Pe = 9 \times 10^3$, $A = 0.46$, $Ga = 2$, and $C = 10^{-5}$ ($Bo_e = 3.73 \times 10^{-4}$); (c) $Pe = 9 \times 10^3$, $A = 0.46$, $Ga = 1$, and $C = 10^{-5}$ ($Bo_e = 7.45 \times 10^{-4}$); (d) $Pe = 9 \times 10^3$, $A = 0.25$, $Ga = 0.1$, and $C = 10^{-5}$ ($Bo_e = 7.45 \times 10^{-3}$).

the vortex-sheet formalism [22]. It is worth mentioning that the value $A = 0.46$ used in the insets (b) and (c) of Fig. 2 is very close to the viscosity contrast values reported in Refs. [14,22], so that the patterns can be directly compared, revealing a remarkable resemblance among them. These findings are reassuring and provide qualitative validations for our diffuse-interface BHSCH numerical simulations.

Further validation of our numerical results is provided by comparing the data for the number of fingers N directly extracted from our numerical experiments with the analytical prediction for N represented by the solid curve in Fig. 2. In general, excellent agreement is observed, especially for increasingly larger values of Bo_e. As stated in Ref. [14], the number of fingers can be more accurately identified for relatively stable interfaces, such as those obtained for higher Bo_e. As expected, for the cases presenting conspicuous nonlinear elements, i.e., finger merging and competition, the linear prediction for N is not as precise. Nevertheless, the overall agreement is still reasonably good.

We proceed by pointing out the usefulness of our diffuse-interface approach in addressing two very important behaviors that arise at nonlinear stages of the dynamics in rotating Hele-Shaw flows: the phenomena of (a) finger competition and (b) droplet pinch-off, and their sensitivity to changes in the value of the viscosity contrast. Weakly nonlinear analysis [15] and sharp interface boundary-integral simulations [16] have verified that competition among fingering structures is considerably modified as A varies: increasingly larger values of $A < 0$ ($A > 0$) lead to enhanced competition among outward (inward) fingers. In addition, it has been found that finger competition is significantly suppressed when $A \to 0$.

These immiscible fluid flow findings have been confirmed by simulations of rotating Hele-Shaw miscible displacements [13], where surface tension effects are mimicked by Korteweg stresses.

Nevertheless, the episodes of finger pinch-off and droplet emissions experimentally captured in Refs. [14,22] can not be properly simulated by sharp interface computational methods employed in Refs. [14,16,17]. This has been accomplished only very recently by Folch and co-workers [22], who derived, analyzed, and implemented a phase-field model based on a vortex-sheet formalism for centrifugally driven Hele-Shaw flows. Their simulations and laboratory experiments for the cases in which $0 \leqslant A \leqslant 1$ demonstrated that pinch-off singularities are more frequent for smaller viscosity contrasts.

However, cases with negative contrast ($A < 0$) and the impact of Coriolis effects on interface singularities have not been addressed in Ref. [22]. For the remainder of this section, we try to further validate our diffuse-interface numerical approach by using it to revisit the advents of finger competition and pinch-off, and their relation to the viscosity contrast (now including negative values of it) in confined rotating flows. The role of the Coriolis force on such phenomena will be studied in Sec. III B.

Before continuing our analysis and presenting more simulations, a few important remarks are in order. It should be noticed that, by design, there exists some interfacial mixing and diffusion in most phase-field models. The acceptable level of interfacial diffusion is very much problem dependent, and the corresponding controlling parameter has to be chosen judiciously [29,30]. In this sense, various scalings for the Péclet number have been suggested in the literature, for instance, $\text{Pe} \sim 1/C$ [31–33] and $\text{Pe} \sim C$ [34]. Taking these points into consideration, and for the safe of consistency, for the rest of this paper, we consider that $\text{Pe} = 9 \times 10^3$. Nonetheless, we point out that the fingering patterns are not significantly altered when different values of Pe are used. For clarity, instead of showing images containing the whole phase-field domain as in Fig. 2, only the contour curve for $c = 0.5$ is plotted in Figs. 3, 5, and 6. This is done without loss of generality.

Another fundamental issue regarding the appropriateness of diffuse-interface models is about the interface, the thickness of which can be approximated as ($O\sqrt{\epsilon}$). To catch an exact interfacial phenomenon in a sharp interface limit, ($O\sqrt{\epsilon}$) → 0 is desired. A guideline regarding the maximum allowable value of the Cahn number had been proposed as $C \sim 10^{-4}$ [46,47], in which the results accurately reflect reality, having molecular scale interfaces. Based on this guideline, we had tested different Cahn numbers between $10^{-4} \sim 5 \times 10^{-6}$ in test simulations, and the overall aspect of the patterns show no significant differences. In this context, we have chosen the smallest value of the Cahn number for which all simulations of interest remain numerically stable: $C = 10^{-5}$. Excellent agreement between our simulated shapes with interfaces obtained in actual experiments validate the appropriateness of our choice for the Cahn number.

It is known that phase-field methods have difficulties in dealing with the particular (but important) case of viscosity contrast $A = 1$ [22], which is actually the easiest to implement experimentally [5], e.g., by choosing air as one of the fluids.
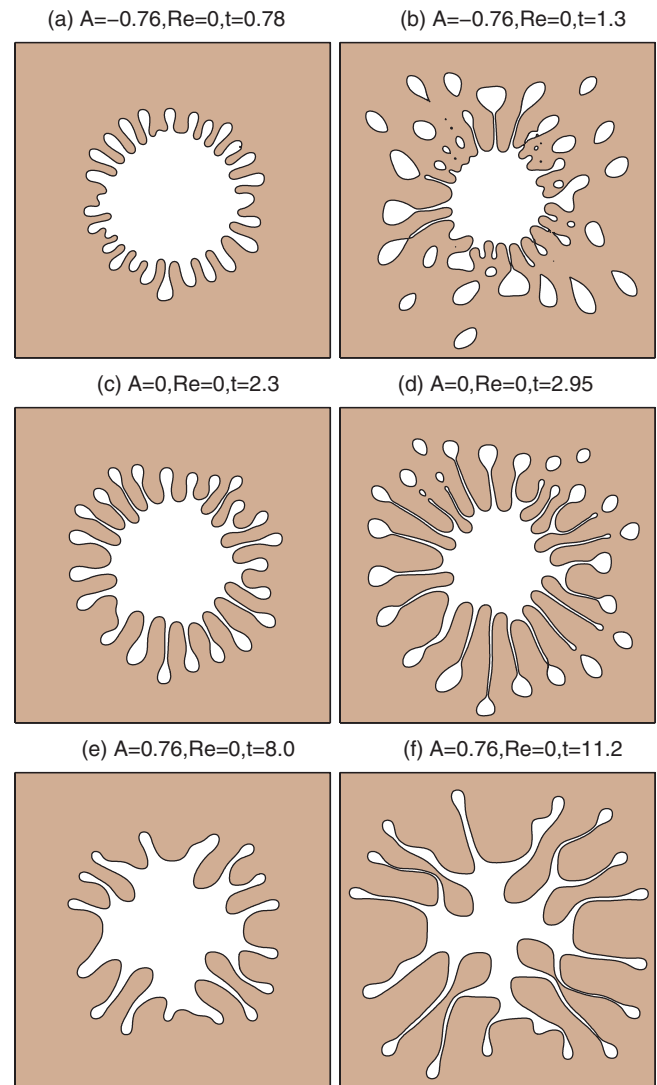

FIG. 3. (Color online) Typical fingering patterns for $A = -0.76$ [(a) and (b)], $A = 0$ [(c) and (d)], and $A = 0.76$ [(e) and (f)]. The remaining parameters are $\text{Pe} = 9 \times 10^3$, $\text{Ga} = 0.4$, and $C = 10^{-5}$ ($\text{Bo}_e = 1.86 \times 10^{-3}$). The left (right) panel shows patterns before (after) the occurrence of pinch-off.

However, simulations for $A = 1$ and -1 are actually not shown in this paper. In fact, we present simulations for the interval $-0.76 \leqslant A \leqslant 0.76$, so that the largest magnitude for the viscosity contrast is 0.76. This is the largest value of A we can simulate for which our numerical code remains stable. Although the whole range of $-1 \leqslant A \leqslant 1$ could not been spanned by our simulations, the particular range of values for the viscosity contrast we consider ($-0.76 \leqslant A \leqslant 0.76$) results in significant fingering, and produce pattern morphologies very close to those obtained through sharp interface methods for higher A [16,20]. Moreover, it is worth noting that fluids with higher density (to allow maximized centrifugal driving) but extremely low viscosity (such as those with A exactly equal to -1) are probably difficult to find in practice. This is the reason why a more realistic value $A = -0.8$ (and not $A = -1$) has been used for the boundary-integral simulations in Ref. [20].

Numerical simulations illustrating the effect of the viscosity contrast on the mechanisms of finger competition and pinch-off are depicted in Fig. 3 for three different values of A: -0.76 [(a) and (b)]; 0 [(c) and (d)]; and 0.76 [(e) and (f)]. First, we focus on the left panel of Fig. 3, which shows characteristic pattern morphologies before the occurrence of complicated pinch-off events. By inspecting Figs. 3(a), 3(c), and 3(e), we observe the formation of distinctly shaped patterns: short petal-like fingers for $A < 0$, stretched filamented structures with bulbous ends for $A = 0$, and more ramified shapes where the width of the fingers do not tend to vary much along their lengths when $A > 0$.

Important information regarding finger competition behavior of the patterns presented on the right column of Fig. 3 can be extracted from Fig. 4, which plots the dimensionless radial coordinate (r) of the tips of both outward and inward moving fingers for each finger (labeled by an integer n) for A: -0.76 [Fig. 4(a)], 0 [Fig. 4(b)], and 0.76 [Fig. 4(c)]. By observing Fig. 4(a) for negative A, it is quite clear that finger length variability (or, finger competition) is very significant for outward moving fingers. Figure 4(c) illustrates just the opposite behavior when $A > 0$, in which inward fingers compete more actively. Inhibition of competition for both inward and outward fingers is also apparent when $A = 0$ [Fig. 4(b)]. All these results, concerned with pattern morphologies and finger competition dynamics, are in very good agreement with similar findings obtained in Refs. [16,20] through sharp interface numerical techniques, and also with weakly nonlinear analytic tools [15].

At this point, we turn to the discussion of the finger pinch-off events depicted on the right panel of Fig. 3. Once again, we focus of the influence of A on this complex phenomenon. An inspection of Figs. 3(b), 3(d), and 3(f) readily leads us to conclude that pinch-off events are increasingly favored for negative viscosity contrast. This occurs because, for $A < 0$, the

interface is both centrifugally and viscosity unstable. Then, the occurrence of pinch-off becomes relatively milder for $A = 0$, and tends to be totally suppressed for large, positive values of A. In addition, we notice that the size of the satellite droplets decreases as A is varied from negative to positive values. Even though the case for $A < 0$ has not been simulated in Ref. [22], our numerical diffuse-interface results for $A \geqslant 0$ are absolutely consistent with their experiments and phase-field simulations.

B. Influence of the Coriolis force

We initiate our analysis of the Coriolis effects by examining Fig. 5. It plots fingering patterns and their corresponding streamlines when Coriolis force is neglected [Figs. 5(a) and 5(b)], and when it is taken into account Figs. 5(c) and 5(d). In Figs. 5(a) and 5(b), $A = 0$ and Re $= 0$, while in Figs. 5(c) and 5(d), $A = 0$ and Re $= 1.1$. Throughout this section, for the simulations including Coriolis effects, we take the maximum allowed value of Re for which our code remains numerically stable.

Note that in Fig. 5 we take a lower value for the equilibrium rotational Bond number $\text{Bo}_e = 7.45 \times 10^{-4}$. Recall that a smaller rotational Bond number represents either weaker surface tension effects or stronger centrifugal driving force, so that the overall interfacial instability is further enhanced. This
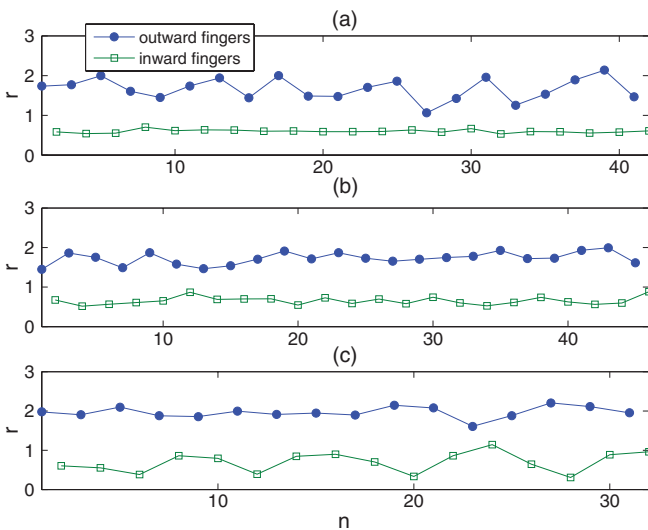

FIG. 4. (Color online) Finger competition behavior for the patterns shown on the left panel of Fig. 3 when (a) $A = -0.76$, (b) $A = 0$, and (c) $A = 0.76$. The dimensionless radial coordinate r of the finger tip is shown for each finger, labeled by an integer number n.
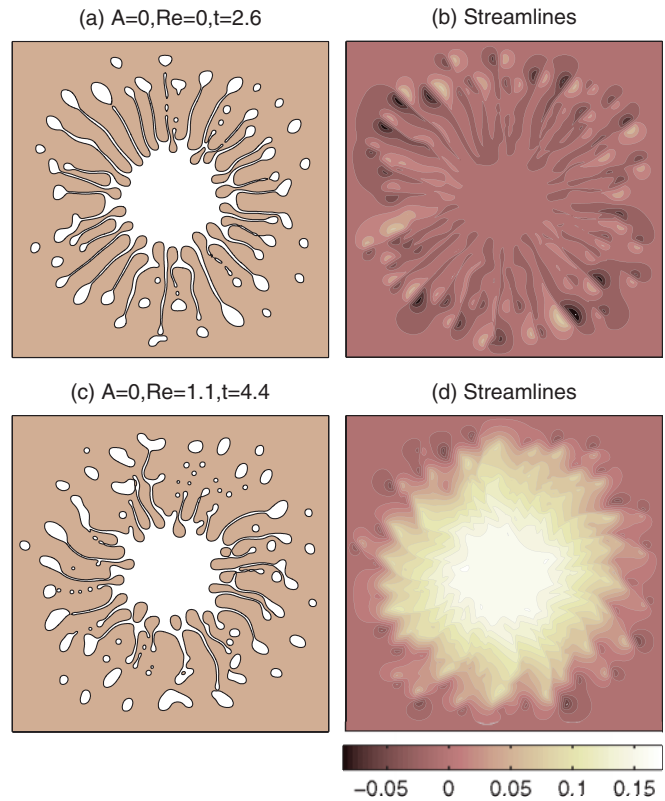

FIG. 5. (Color online) Fingering patterns and streamlines for Pe $= 9 \times 10^3$, Ga $= 1$, and $C = 10^{-5}$ ($\text{Bo}_e = 7.45 \times 10^{-4}$) for $A = 0$ and Re $= 0$ [(a) and (b)]; $A = 0$ and Re $= 1.1$ [(c) and (d)]. The magnitudes of the streamlines are represented by the color coding presented in the horizontal bar at the bottom. The streamlines are plotted in equal intervals of the stream function.

is clearly seen by contrasting Fig. 5(a) with Fig. 3(d). Also plotted in Fig. 5(b) are the corresponding streamlines with their strengths indicated according to the background color coding (see horizontal bar at the bottom of the figure). In line with the results of conventional viscous fingering [21,38], each finger consists of a pair of countercirculating eddies. These countercirculating eddies possess roughly equal strengths, but different signs, with their maxima ($\phi \approx \pm 0.086$) located at the fingertips. As expected, the overall flow depicted in Figs. 5(a) and 5(b) is mainly in the radial direction.

The main morphological features induced by the Coriolis force can be easily identified in Figs. 5(c) and 5(d). If, on one hand, the pattern shown in Fig. 5(a) grows along the radial direction, on the other hand, the central body of the drop in Fig. 5(c) looks rotated (or, "phase drifted" [20]), clearly exhibiting finger bending phenomena. It is also noticeable that the number of fingers is reduced, while their growth is slowed down. Conversely, it is important to observe that finger pinch-off events and droplet emissions are more frequent when Coriolis force effects are considered. Most of these findings can be understood by the fact that, contrary to the centrifugal force, the Coriolis force acts along the azimuthal direction, restraining radial grow, and favoring the tilting of the emerging fingers. Enhanced pinch-off can be attributed to inertia since the Coriolis force tends to move the unstable finger backward, favoring finger breakup and droplet detachment.

Further realization about the influence of the Coriolis force can be obtained by the streamlines depicted in Fig. 5(d). Instead of numerous separated eddy pairs, which appear in Fig. 5(b), the streamlines of all the fingers in Fig. 5(d) are connected through the formation of multilayers. These streamlines indicate the significant presence of azimuthal velocities. The stabilization of finger growth can also be quantitatively evaluated by the lower local maximum strength of stream function ($\phi \approx \pm 0.057$) at the fingertips. On the other hand, the strength of the stream function is much higher at the central region of the main drop, which means a significant fluid rotation. It is this azimuthally directed flow that is responsible for the rotational behavior of the drop's body.

The tangential shear induced by azimuthal velocity variations along the radial direction can also be noticed in Fig. 5(d). Since the streamlines are plotted in equal intervals of the stream function, the magnitudes of velocities are represented by the density of local streamlines. It is apparent that the largest azimuthal velocities are induced at the rim region, and reduced inwardly. A strong tangential shear is generated by this velocity variation. The larger magnitude of the azimuthal velocity at the outer rim explains the bending of the fingers. Moreover, the tangential shear is the cause of enhanced finger pinch-off and droplet emissions.

We advance by analyzing Fig. 6, which depicts fingering patterns and their corresponding streamlines when $A = 0$ and $Re = 1.1$ [Figs. 6(a) and 6(b)]; $A = 0.46$ and $Re = 1.6$ [Figs. 6(c) and 6(d)]; and $A = 0.76$ and $Re = 1.6$ [Figs. 6(e) and 6(f)]. The rest of the parameters are the same as those presented in Fig. 3. However, in contrast to what we did in Fig. 3, we do not address the case $A = -0.76$ in Fig. 6. Unfortunately, when $A = -0.76$, the maximum Reynolds number we could successfully simulate was only $Re = 0.23$. Coriolis force effects are insignificant for this low Reynolds
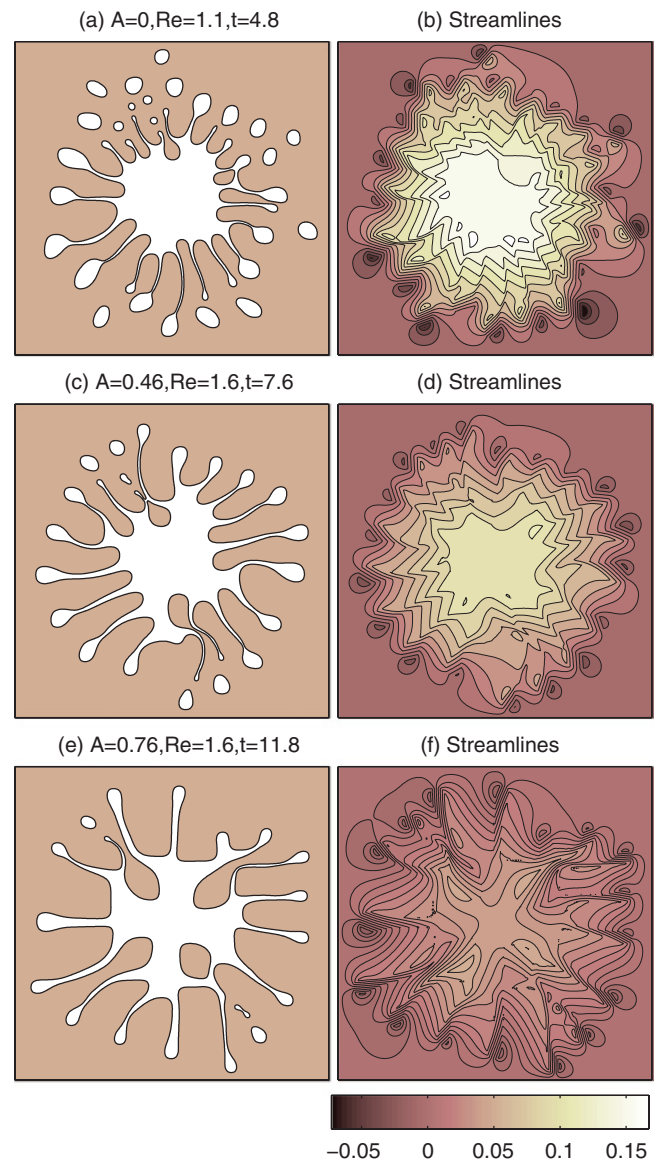

FIG. 6. (Color online) Fingering patterns and corresponding streamlines when Coriolis force effects (tuned by the Reynolds number Re) are taken into account for $A = 0$, $Re = 1.1$ [(a) and (b)]; $A = 0.46$, $Re = 1.6$ [(c) and (d)]; and $A = 0.76$, $Re = 1.6$ [(e) and (f)]. The values of the parameters Pe, Ga, C, and Bo_e are the same as those utilized in Fig. 3.

number value within the time period of the simulation, thus, this case is not really illustrative, so it is not shown.

The fingering patterns for $A = 0$ and 0.76, shown in Figs. 6(a) and 6(e), can be directly compared with the equivalent cases without the Coriolis force shown in Figs. 3(d) and 3(f). Consistent with the results presented earlier in this section, Coriolis force effects lead to damped radial growth plus enhanced emission of satellite droplets. In particular, notice that while there is no pinch-off in Fig. 3(f), it does arise in Fig. 6(e). Plots for an intermediate value of the viscosity contrast ($A = 0.46$) are shown in Figs. 6(c) and 6(d), confirming the trend that even in the presence of Coriolis effects, pinch-off is indeed more frequent when $A \to 0$. One can also notice the occurrence of finger merging in

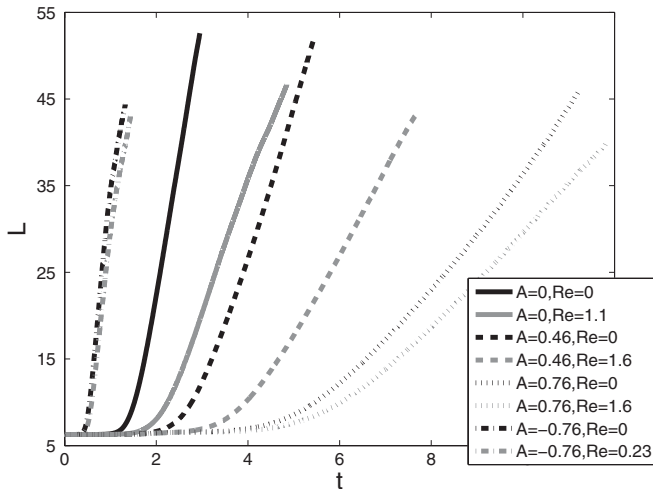FIG. 7. Time evolution of the interfacial length L for various viscosity contrasts and Reynolds numbers. Here, $\text{Pe} = 9 \times 10^3$, $\text{Ga} = 0.4$, and $C = 10^{-5}$ ($\text{Bo}_e = 1.86 \times 10^{-3}$).

Figs. 6(a), 6(c), and 6(e) induced by Coriolis effects. This creates "islands" of fluid 1 surrounded by fluid 2.

Further examination of Fig. 6 reveals other noteworthy facts. While strong finger bending, accompanied by some drop rigid rotation, occurs for $A = 0$ [Fig. 6(a)], rigid rotation seems to be the dominant phenomenon if $A = 0.76$ [Fig. 6(e)]. On the other hand, for an intermediate viscosity contrast value $A = 0.46$ [Fig. 6(c)], both tilting of the fingers and rotation of the drop body can be observed.

These distinct behaviors can also be understood with the help of the streamlines plotted in Figs. 6(b), 6(d), and 6(f). Similar to the case studied in Fig. 5(d), here the streamlines are more circular, presenting larger azimuthal velocities near the fingertips, for smaller values of the viscosity contrast. The circular streamlines indicate that the whole drop's body is subjected to a rotational motion. The bending of the fingers results from the faster movements taking place at the fingertips. On the other hand, the streamlines present significant radial orientation at areas closer to the fingers' roots for larger values of A ($A = 0.76$). In this case, the streamlines are almost evenly distributed, which implies a nearly uniform circulating flow field. The existence of nearly uniform azimuthal velocities explains a more prominent rigid rotation of the whole fluid.

We conclude by presenting Fig. 7, which provides complementary information about the role played by the Coriolis effects. It plots the pattern's interfacial lengths as a function of time, for different values of A and Re. In agreement with our previous observations, we see that the inclusion of the Coriolis force leads to interfacial stabilization, resulting in shorter lengths. It is also apparent that the effect to a negative $A = -0.76$ is not that significant, at least in the time period simulated. Finally, for a fixed value of the Reynolds number (say, for Re $= 1.6$), it can be observed that Coriolis effects are more intense for a smaller viscosity contrast ($A = 0.46$). All these findings are consistent with existing sharp interface numerical results [20].

IV. CONCLUSION

We have presented a diffuse-interface numerical study for the rotating Hele-Shaw problem, which has been implemented by utilizing a Boussinesq Hele-Shaw-Cahn-Hilliard (BHSCH) approach. Our analysis considers the role of negative, zero, and positive viscosity contrast, as well as the action of Coriolis force effects.

In the absence of Coriolis effects, our results correctly predict the number of emergent fingering structures, and the appropriate finger competition behavior as the viscosity contrast A is varied. We have also found that the occurrence of complex finger pinch-off events are increasingly favored as A changes from positive to negative values. The excellent agreement between our numerical results with existing experiments [14,17,22], spectral method [13], boundary integral [16], and a different kind of phase-field simulation [22], plus analytical calculations [15], serve to substantiate the validity and correctness of our BHSCH approach.

When Coriolis force contributions are taken into account, our numerical experiments clearly reveal three basic behaviors: a stabilized radial growth, existence of pattern phase drift, and development of finger bending. Once again, all these features are in line with what has been obtained by previous simulational investigations of the problem, which employed distinct numerical techniques [20,21]. Furthermore, we have also verified that important topological changes related to finger pinch-off and emission of satellite droplets are significantly favored by the action of the Coriolis force.

[1] P. G. Saffman and G. I. Taylor, Proc. R. Soc. London A **245**, 312 (1958).

[2] L. Paterson, J. Fluid Mech. **113**, 513 (1981).

[3] J. Casademunt, Chaos **14**, 809 (2004).

[4] L. W. Schwartz, Phys. Fluids A **1**, 167 (1989).

[5] Ll. Carrillo, F. X. Magdaleno, J. Casademunt, and J. Ortín, Phys. Rev. E **54**, 6260 (1996).

[6] V. M. Entov, P. I. Etingof, and D. Ya. Kleinbock, Eur. J. Appl. Math. **6**, 399 (1996).

[7] F. X. Magdaleno, A. Rocco, and J. Casademunt, Phys. Rev. E **62**, R5887 (2000).

[8] D. Crowdy, Q. Appl. Math. **60**, 11 (2002).

[9] J. A. Miranda, H. Gadêlha, and A. T. Dorsey, Phys. Rev. E **82**, 066306 (2010).

[10] E. Alvarez-Lacalle, J. Ortín, and J. Casademunt, Phys. Rev. Lett. **92**, 054501 (2004).

[11] E. S. G. Leandro, R. M. Oliveira, and J. A. Miranda, Phys. D (Amsterdam) **237**, 652 (2008).

[12] C.-Y. Chen and S.-W. Wang, Fluid Dyn. Res. **30**, 315 (2002).

[13] C.-Y. Chen, C.-H. Chen, and J. A. Miranda, Phys. Rev. E **73**, 046306 (2006).

[14] E. Alvarez-Lacalle, J. Ortín, and J. Casademunt, Phys. Fluids **16**, 908 (2004).

[15] H. Gadêlha and J. A. Miranda, Phys. Rev. E **70**, 066308 (2004).

[16] J. A. Miranda and E. Alvarez-Lacalle, Phys. Rev. E **72**, 026306 (2005).

[17] E. Alvarez-Lacalle, J. Ortín, and J. Casademunt, Phys. Rev. E **74**, 025302(R) (2006).

[18] S. Ramezani, S. Aniss, and M. Souhar, C. R. Mec. **330**, 633 (2002).

[19] S. L. Waters and L. J. Cummings, Phys. Fluids **17**, 048101 (2005).

[20] E. Alvarez-Lacalle, H. Gadêlha, and J. A. Miranda, Phys. Rev. E **78**, 026305 (2008).

[21] C.-Y. Chen, C.-W. Huang, H. Gadêlha, and J. A. Miranda, Phys. Rev. E **78**, 016306 (2008).

[22] R. Folch, E. Alvarez-Lacalle, J. Ortín, and J. Casademunt, Phys. Rev. E **80**, 056305 (2009).

[23] D. P. Jackson and J. A. Miranda, Phys. Rev. E **67**, 017301 (2003).

[24] R. Folch, J. Casademunt, A. Hernández-Machado, and L. Ramírez-Piscina, Phys. Rev. E **60**, 1724 (1999).

[25] R. Folch, J. Casademunt, A. Hernández-Machado, and L. Ramírez-Piscina, Phys. Rev. E **60**, 1734 (1999).

[26] R. Folch, J. Casademunt, and A. Hernández-Machado, Phys. Rev. E **61**, 6632 (2000).

[27] D. Anderson, G. B. McFadden, and A. A. Wheeler, Annu. Rev. Fluid Mech. **30**, 139 (1998).

[28] J. W. Cahn and J. E. Hilliard, J. Chem. Phys. **28**, 258 (1958).

[29] D. Jacqmin, J. Comput. Phys. **155**, 96 (1999).

[30] P. Yue, J. Feng, C. Liu, and J. Shen, J. Fluid Mech. **515**, 293 (2004).

[31] J. Lowengrub and L. Truskinovsky, Proc. R. Soc. London, Ser. A **454**, 2617 (1998).

[32] H.-G. Lee, J. Lowengrub, and J. Goodman, Phys. Fluids **14**, 492 (2002).

[33] H.-G. Lee, J. Lowengrub, and J. Goodman, Phys. Fluids **14**, 514 (2002).

[34] M. Verschueren, Ph.D. thesis, Technische Universiteit Eindhoven, the Netherlands, 1999.

[35] C. Glasner, Nonlinearity **16**, 49 (2003).

[36] A. Vorobev, Phys. Rev. E **82**, 056312 (2010).

[37] H. Hu and D. Joseph, Z. Angew. Math. Phys. **43**, 626 (1992).

[38] C.-Y. Chen and H.-J. Wu, Phys. Fluids **17**, 042101 (2005).

[39] C.-Y. Chen and E. Meiburg, J. Fluid Mech. **371**, 233 (1998).

[40] M. Ruith and E. Meiburg, J. Fluid Mech. **420**, 225 (2000).

[41] E. Meiburg and C.-Y. Chen, SPE J. **5**, 129 (2000).

[42] C. T. Tan and G. M. Homsy, Phys. Fluids **31**, 1330 (1988).

[43] P. Petitjeans and T. Maxworthy, J. Fluid Mech. **326**, 37 (1996).

[44] P. Petitjeans, C.-Y. Chen, E. Meiburg, and T. Maxworthy, Phys. Fluids **11**, 1705 (1999).

[45] J. Kuang, T. Maxworthy, and P. Petitjeans, Eur. J. Mech. B: Fluids **22**, 271 (2003).

[46] P. Yue, C. Zhou, J. J. Feng, C. F. Ollivier-Gooch, and H. H. Hu, J. Comput. Phys. **219**, 47 (2006).

[47] C. Zhou, P. Yue, J. J. Feng, C. F. Ollivier-Gooch, and H. H. Hu, J. Comput. Phys. **229**, 498 (2010).